Check for updates

ChemElectroChem

Research Article
doi.org/10.1002/celc.202300168

Chemistry Europe
European Chemical Societies Publishing

www.chemelectrochem.org

Special Collection

Super Hygroscopic Non-Stoichiometric Cerium Oxide Particles as Electrode Component for PEM Fuel Cells

Lucia Mazzapioda,*[a] Gabriele Moscatelli,[a] Nicholas Carboni,[a] Sergio Brutti,[a] and Maria Assunta Navarra*[a, b]

The design of highly efficient promoters for the oxygen reduction reaction (ORR) is an important challenge in the large-scale distribution of proton exchange membrane (PEM) fuel cells. Hygroscopic cerium oxide (CeO_2) is here proposed as co-catalyst in combination with Pt. Physical chemical characterizations, by means of X-ray diffraction, vibrational spectroscopy, morphological and thermal analyses, were carried out, demonstrating high water affinity of the synthesized CeO_2 nanoparticles. Composite catalysts (i.e., Pt:CeO_2 1:0.5 and 1:1 wt: wt), were studied by either rotating disk electrode (RDE) and fuel cell tests performed at 80 °C and 110 °C. Interestingly, the cell adopting the Pt:CeO_2 1:0.5 catalyst enabled the achievement of high power densities reaching ~80 and ~35 mW cm^{-2} under low relative humidity and high temperatures. This result demonstrates that tuning material surface properties (e.g. oxygen vacancies) could significantly boost the electrochemical performance of cathodes as a combined result of optimized water retention and improved ORR kinetic.

Introduction

In recent years, hydrogen is receiving a renewed and considerable attention in Europe and around the world thanks to its many applications in industry, transport, power sectors.[1,2] Most importantly, it can be considered a promising solution to decarbonize industrial processes because it does not emit air pollution, especially CO_2, when used offering a cardinal support to economic sectors to reduce carbon emissions. In this context, PEM fuel cells are an efficient conversion technology which allows to use hydrogen as a clean energy carrier producing clean electricity.[3–5] The key component of these devices is the Membrane Electrode Assembly (MEA), which consists of polymer electrolyte membrane interposed between the anode and cathode electrodes. At the current stage in technology, platinum (Pt)-based materials and the Nafion® (DuPont™) are commonly used as catalyst and electrolyte respectively.[6,7] Despite, several automobile industries have commercialized PEMFCs-based vehicles, the stability of both catalyst and

electrolyte materials represent a huge hurdle to improve the overall cell performances and life.[8,9] During fuel cell operations, three main degradation mechanisms occur: thermal degradation, mechanical degradation, and chemical degradation. Among all, the chemical degradation represents the main issue that influences the lifespan of a fuel cell.[10–12] Specifically, the hydrogen peroxide (H_2O_2) and the active radical species generated during fuel cell operations, attack the functional groups of the membrane and/or ionomer molecules present in the catalyst layers, affecting the electrolyte structure and causing its deterioration.[13,14] This phenomenon becomes faster under stringent operating conditions, such as low relative humidity (RH), because the presence of peroxide groups in absence of water promotes the crossover of fuel and oxidant through the electrolyte generating pinholes and cracks inside the Nafion membrane, leading to its degradation.[15–16] If on one hand, water is a fundamental element to improve the stability of both electrolyte and electrode components, on the other hand industry players are pushing the development of PEMFCs capable to work under lower humidity condition. This would entail the removal of the external humidification systems with the beneficial reduction of the fuel cell system costs. Therefore, develop radical scavengers inside PEMs and/or in the catalyst layer, which can work against the radical attacks to obtain durable PEMFC performance under low RH, is challenging. Several studies have found that CeO_2 can act as a promising scavenging system thanks to its reversible redox reaction between Ce^{3+} and Ce^{4+} with a consumption of both radicals and peroxides species. In detail, this scavenging reaction takes place in a cyclic reaction path where Ce^{3+} ions consume hydroxyl radicals producing water molecules and Ce^{4+} ions. In the second step, Ce^{4+} reacts with hydrogen peroxide and peroxide radicals reproduce Ce^{3+} ions back.[17–20] This redox cycling which promotes reversible stoichiometric storing (CeO_2) and release of oxygen ($CeO_{2-\delta}$), is attributed to the formation of oxygen vacancies in the ceria's lattice structure. These vacancies

[a] Dr. L. Mazzapioda, G. Moscatelli, N. Carboni, Prof. S. Brutti, Prof. M. A. Navarra
Department of Chemistry,
Sapienza University of Rome,
Piazzale Aldo Moro 5, 00185 Rome (Italy)
E-mail: lucia.mazzapioda@uniroma1.it
mariassunta.navarra@uniroma1.it
[b] Prof. M. A. Navarra
Hydro-Eco Research Center
Sapienza University of Rome
Via A. Scarpa 16, 00161 Rome (Italy)

depend on the concentration of Ce^{3+} ions on the surface of CeO_2, which governs the antioxidant activity.[21] Thanks to its unique property, CeO_2 has been investigated as a promoter of the Pt/C catalyst for enhancing the oxygen concentration on the cathode surface and the ORR catalytic activity, leading to increase low-temperature fuel cell performances. The enhanced performance obtained with the CeO_2 addition in the cathode layer is also due to the strong interaction between Pt and the oxide particles and to a better stability and durability of the composite catalysts.[22–25] However, it was demonstrated that cerium ions can get soluble in water during fuel cell operation, migrating out of the ionomer or binder, resulting in the loss of scavenging effect. In addition, these positive cerium ions (Ce^{3+} or and Ce^{4+}) in water can establish ionic interaction with the anionic sulfonic groups of the membrane, reducing its proton conductivity.[26,27]

Here we propose the use of a hygroscopic non-stoichiometric CeO_2 oxide as promoter of the Pt/C catalyst with the aim to improve cell performances, especially the ORR activity, under high temperature and low RH. Compared with previous studies about CeO_2 and Pt/C:CeO_2 composite catalysts, the novelty of this work lies in the peculiar super hydrophilicity of the proposed CeO_2 additive, which plays a crucial role in optimizing both water drainage and the cathode and electrolyte interface, resulting in a remarkable improvement in Nafion proton conductivity. For the first time, it was demonstrated that the use of such a defective super hygroscopic ceria additive allows better fuel cell performances, with respect to benchmark Pt/C catalyst, at high temperatures (80 °C and 110 °C) and low relative humidity (31 %), which reflect the desired working conditions.

Results and Discussion

The X-ray diffraction (XRD) pattern of the synthesized cerium oxide (CeO_2) is depicted in Figure 1, where the seven major peaks indexed as (111), (002), (022), (113), (133), (024) and (442) correspond to a single phase of CeO_2 with a cubic structure and space group Fm-3 m (ICSD n°55284 phase, blue curve) as reported elsewhere.[28] The average crystal size of the sample, determined by Maud code, is found to be $16,5 \pm 0,09$ nm.

The morphological structure of the additive has been revealed by SEM analysis, recorded at two different magnifications, as shown in Figure 2. Clearly, the powder is composed by micrometric aggregates made up of smaller particles in the nanometric range, in agreement with the crystallite size evaluation above.

Based on Brunauer–Emmett–Teller (BET) analysis, the surface area is found to be 55 $m^2 g^{-1}$. The total volume of pores is 0,0828 cm^3/g.

The additive was also characterized by Infrared spectroscopy (Figure 3, left); prior to the measurement, the sample was dried at 80 °C overnight to remove physiosorbed water. The FTIR spectrum is reported in Figure 3 where the band of cerium oxide, in particular the peak at 510 cm^{-1} due to O—Ce—O
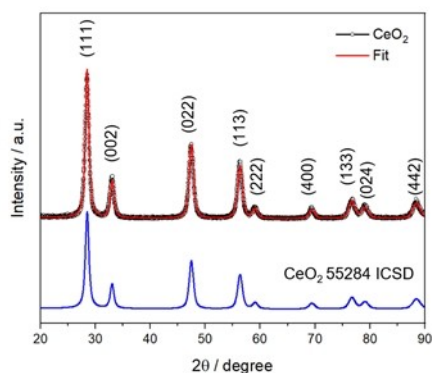

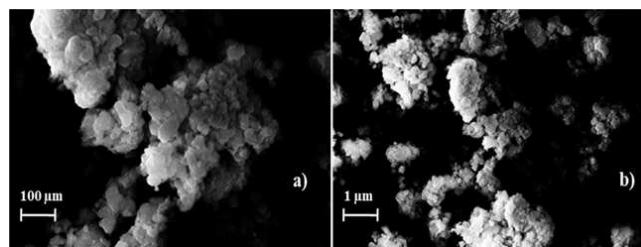**Figure 1.** X-ray diffraction pattern of the synthesized CeO_2 powder.

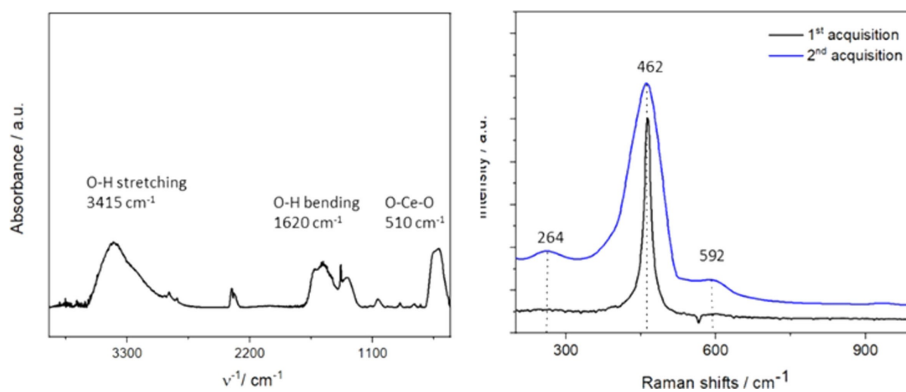**Figure 2.** SEM images of the synthesized CeO_2 powder at a) 100kX and b) 35kX magnification.

Figure 3. Infrared (on the left) and Raman (on the right) spectra of CeO_2 powder.

ChemElectroChem

Research Article
doi.org/10.1002/celc.202300168

Chemistry
Europe
European Chemical
Societies Publishing

stretching mode of vibration, is recognized.[29] Despite the drying treatment, the typical bands related to the absorbed water on the oxide surface are observed. A large peak at $3415\ cm^{-1}$, attributed to the stretching vibration of O—H groups, and the bending of O—H groups at 1350 and $1650\ cm^{-1}$, are found. It is worth noticing that these last bands are large and complex, suggesting a peculiar O—H groups absorption/coordination on the cerium oxide surface.[30]

More detailed structural information on cerium oxide was obtained using a confocal Raman microscope (Figure 3, right). The sample was characterized after drying it at 80 °C under vacuum for one night. Two subsequent acquisitions were recorded. It is interesting to note that in the first spectrum acquired (black curve), only one main peak, corresponding to the symmetric stretching of the Ce—O vibrational unit (fluorite structure, F_{2g}) at $462\ cm^{-1}$, is clearly visible. This confirms the crystallization of well-formed ceria crystallites. However, two additional vibrational modes, centered at 264 and $594\ cm^{-1}$, are evident in the second spectrum acquired (blue curve), due to the second-order transverse acoustic (2TA) mode and the defect-induced (or oxygen vacancy) mode respectively.[31] It is important to recall that the change in shape and intensity of the band at $462\ cm^{-1}$ is typically related to an inhomogeneous strain effect due to variations in particle size and morphology, thus explaining the changes between the two consecutive spectral acquisitions. On the other hand, the shift and broadening of the peak at $594\ cm^{-1}$, which in our case falls at higher Raman frequencies, are due to alterations of oxygen vacancies at the surface and within the oxide lattice.[32,33] Other Raman studies on CeO_2 oxide[34,35] suggest that heat treatments lead to evident modifications of the $594\ cm^{-1}$ peak shape, which becomes less asymmetric while increasing the drying temperature. Consequently, we can speculate that, when ceria is heated by the Raman laser, local structural rearrangements take place induced by the loss of chemisorbed water molecules, leading to formation of the oxygen vacancies in the lattice.

The thermal stability of the additive was evaluated by thermal gravimetric analysis (TGA). The TGA profile shown in Figure 4, confirms the high hygroscopicity of the powder with a total mass loss, due to the dehydration phenomena, of about 5,5 %. From the derivative curve (DTG, red curve in Figure 4), two distinct weight losses are detected in the low-temperature

range: the first stage at about 75 °C is due to the removal of surface water and another one, at 130 °C, is attributed to water molecules strongly adsorbed on the cerium oxide surface. This aspect could justify the results obtained by both FTIR and Raman analysis related to the water coordination on the oxide lattice.

Following the procedure described in paragraph 2.2, the Oxygen Capacity Storage (OCS) of the cerium oxide particles was evaluated by TGA, as reported in Figure 4b. From the thermogravimetric curve, it is demonstrated that the additive is able to storage/release oxygen only in dehydrated state exhibiting a high OCS value, ca. 6 %. Unfortunately, this capacity fails under standard conditions, because of the highest hygroscopicity of the additive. This behavior can be explained considering the well-known ion-incorporation reactions at the ceria—gas interface due to the presence of oxygen vacancies in the lattice of the oxide.[36,37] Based on these studies, the incorporation of hydroxyl ions on surface oxygen vacancies is faster compared to an oxygen adsorption, leading to the complete coverage/saturation of cerium oxide surface with water molecules. Furthermore, it was demonstrated that the formation of oxygen vacancies is facilitated with the decrease of CeO_2 particles size which reduces the coordination atoms of oxygen in CeO_2, enhancing the coordinative unsaturation of cerium cations and improving the polar character of the surface of CeO_2.[38] As a consequence, these cerium cations, as well as surface oxygen vacancies, have a higher tendency to exchange electrons with interfacial water molecules.[39,40]

Thereby, we can assume that the interactions between water molecules and defective CeO_2 surface introduce a super hydrophilic wetting behaviour for such a defective CeO_2 surface, making the OCS negligible.

Figure 5 shows the 5th CV curves, recorded after the conditioning procedure, for all the investigated catalysts, where both hydrogen adsorption/desorption processes in the region 0.05–0.4 V vs RHE and platinum redox reactions in the range 0.4–1.1 V vs RHE are clearly visible.

To have an idea of the catalytic activity of the different catalyst compositions, the electrochemically active surface area (ECSA) was calculated and reported in Table 1. Specifically, the ECSA values were derived by integrating the H-adsorption peak, in the 0.4–0.05 V vs. RHE potential range, corrected for the
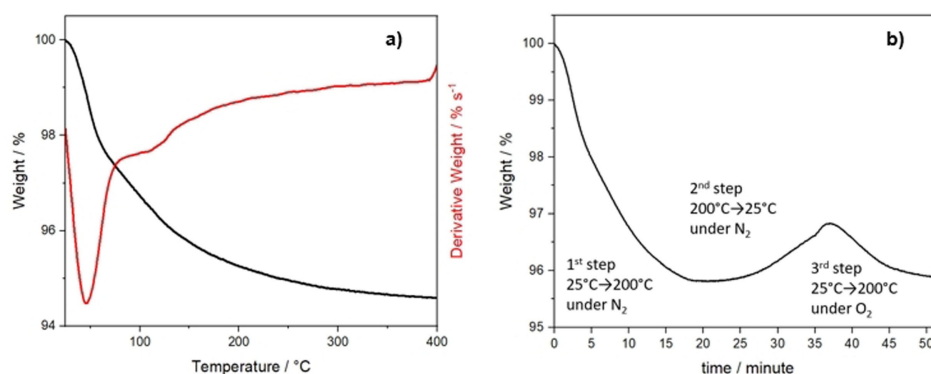

Figure 4. a) TG/DTG and b) oxygen storage capacity (OSC) analysis of the synthesized CeO_2 powder.
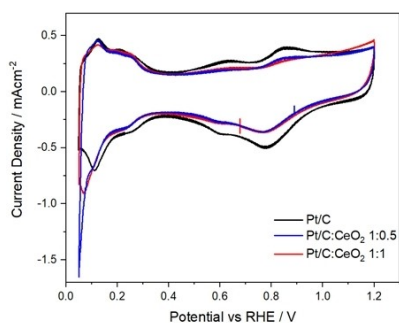
ChemElectroChem

Research Article
doi.org/10.1002/celc.202300168

Chemistry Europe
European Chemical
Societies Publishing

Figure 5. CV profiles of all the catalyst samples recorded under nitrogen flux at 20 mV s^{-1}.

Table 1. Electrochemically active surface area (ECSA) values for the various catalyst compositions.

Sample	ECSA/[m^2 g^{-1}]
Pt/C	63,6
Pt/C:CeO$_2$ 1:0.5	65,0
Pt/C:CeO$_2$ 1:1	80,7

double-layer charging contribution. It is seen that all composite catalysts exhibit higher ECSA values than the benchmark Pt/C catalyst, with the highest value (80,7 m^2 g^{-1}) for the Pt/C:CeO$_2$ 1:1 composition.

These results can be explained reasonably by SEM images of the catalyst inks taken to analyze the particles distribution and morphology of the ink deposition before the electrochemical characterizations (Figure S1). As reported from the images, the CeO$_2$ particles results more uniformly distributed and homogeneous in Pt/C:CeO$_2$ 1:1 sample, rendering the ink surface more compact. On the contrary, small and uneven particles agglomeration is clearly visible in the Pt/C:CeO$_2$ 1:0.5 ink depositions. The element mapping, reported in Figure S2 for both the composite catalysts, confirms the uniform distribution of Ce in the Pt/C:CeO$_2$ 1:1 electrode, justifying the increase in active surface area due to the effectiveness of the CeO$_2$ surface coverage on the Pt electrode.

These results are in agreement with those reported by Tasdemir and coworkers, who observed an improvement of ECSA by the addition of CeO$_2$ particles to the Pt/C catalyst and reported a strong enhancement in terms of current density for both hydrogen and Pt processes when Pt/C–CeO$_2$ was used.[41] As visible from CV curves in Figure 5, our composite catalysts show a reduction of intensity for both Pt peaks and an enhancement, followed by a backward shift, of H$^+$ desorption peaks especially for Pt/C:CeO$_2$ 1:0.5 sample. Fugane et al.[42] have reported CVs of Pt–CeO$_x$/C catalysts where the characteristic peaks of oxidation and reduction of Pt were absent, showing only desorption and adsorption of H$^+$ on Pt. These results were explained considering a partial coverage of Pt surface by ceria layer, which inhibited the oxidation of Pt in cathodic condition. Masuda et al.,[43] who studied the ORR interface on Pt–CeO$_x$/C by using X-ray absorption fine structure (XAFS), demonstrated that the Ce^{3+} was oxidized to Ce^{4+} instead of Pt at the Pt-oxide formation potential (0.9 V).

Apparently, Pt oxide formation was suppressed by the electrochemical redox reaction of cerium species. Moreover, Mori and coworkers observed H$^+$ desorption process in back sweep with respect to Pt/C catalyst suggesting a modulation of the electronic structure of Pt induced by the presence of CeO$_x$.[44] Based on these observations, we can suppose that the improvement of the catalytic activity for all composite catalysts can be attributed to a positive interaction between platinum clusters and CeO$_2$ particles. As a result of this interaction, the availability of active sites on Pt surface results enhanced thanks to the effect of the redox reaction of cerium oxide (Ce^{3+}↔Ce^{4+}), leading to an improvement of ECSA. Therefore, the electrocatalytic properties of composite catalysts are expected to improve increasing the amount of the inorganic additive.

The oxygen reduction reaction (ORR) activity was examined by rotating disk electrode (RDE) experiments at different rotation speeds per minute (rpm) in O$_2$-saturated 0.1 M HClO$_4$ (Figure S3). As shown in Figure 6, where the comparison among different catalyst compositions is reported at 1600 rpm, all catalysts display nearly identical onset potential (E$_{onset}$) for the ORR determined at −0,1 mA cm^{-2}.[44] In detail, for both the Pt/C and Pt/C:CeO$_2$ 1:0.5 compositions, E$_{onset}$ is found to be 0.95 V, whereas for the Pt/C:CeO$_2$ 1:1 the ORR E$_{onset}$ is shifted positively to 0.99 V.

As well-known, the half-wave potential (E$_{1/2}$) which reflects the coupling behavior of surface reaction and mass diffusion is generally used to evaluate the activity of the electrocatalysts.[45] It is interesting to note that the half-wave potential of Pt/C:CeO$_2$ 1:0.5 is shifted toward lower potential with respect to the other samples, indicating a lower capability of this catalyst in reducing the ORR overpotential. However, the limiting current density, j$_d$, is higher for the composite catalysts compared to plain Pt/C; especially, the Pt/C:CeO$_2$ 1:1 sample exhibits the highest j$_d$ reaching a value lower than −6 mA cm^{-2}. If one considers that in the low potential region (the so-called mass diffusion region), the ORR is dominated by O$_2$ diffusion on the electrode surface,[46] we can assume that the oxygen storage ability of CeO$_2$ increases the oxygen concentration on Pt surface, improving the ORR activity. Liam et al. suggested that the oxygen supplied from cerium oxide to Pt surface can contribute to the enhancement of the ORR activity of the Pt–CeO$_x$ cathode.[47] In addition, as explained before for CV results, the ability of cerium oxide to modify the electro-
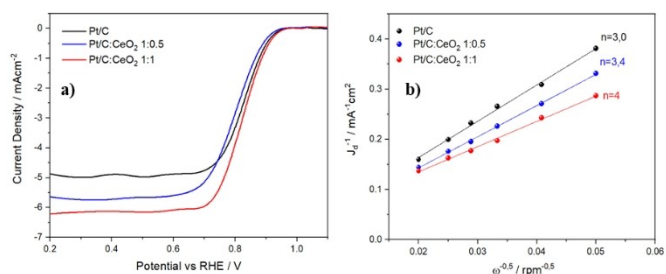

Figure 6. a) Oxygen reduction polarization curves at 1600 rpm in O$_2$-saturated 0.1 M HClO$_4$ at 5 mV s^{-1} and b) Koutecky-Levich plots for Pt/C, Pt/C:CeO$_2$ 1:0.5 and Pt/C:CeO$_2$ 1:1 samples.

ChemElectroChem

Research Article
doi.org/10.1002/celc.202300168

**Chemistry
Europe**
European Chemical
Societies Publishing

chemical oxidation of Pt at 0.9 V needs to be taken into account. The inhibition of Pt-oxide formation, because of the oxidation of cerium ions, makes Pt surface available and more active for the ORR than in bare Pt/C surface. The ORR rate results enhanced, and this effect is optimized by the presence of the oxygen vacancies on the Pt–CeO$_2$ interface.[48,49]

The Koutecky-Levich reciprocal plots constructed considering the diffusion-controlled region at E = 0.3 V vs. RHE at different rotation speed, are shown in Figure 6b. As expected for a kinetically limited process, these plots are linear with a non-zero intercept, indicating that the kinetic limitations are not derived from slow charge diffusion of oxygen through the catalytic film otherwise they would result into non-linearity.[50] The number of electrons exchanged during the ORR was estimated and reported in the same Figure 6b. As well known, ORR can occur by two pathways: the direct four-electron transfer pathway from O$_2$ to H$_2$O and the two-electron transfer pathway from O$_2$ to hydrogen peroxide. The Pt/C:CeO$_2$ 1:1 composition shows the perfect ORR performance with a four-electron pathway whereas the other two samples seem to be less efficient towards the 4e$^-$ pathway. These results could be still attributed to the presence of oxygen defects on the CeO$_2$ structure which can create new oxygen adsorption pathway on the metal-oxide particles surface promoting the oxygen reduction reaction to proceed through the four-electron reduction pathway.[51] In accordance with the ECSA data reported in Table 1, we have recognized the composite Pt/C:CeO$_2$ 1:1 sample as the most active catalyst among all those here investigated.

Both composite catalysts were investigated at the cathode side of a PEM fuel cell, maintaining the same weight ratio between Pt and cerium oxide used for RDE analysis. For sake of comparison, a bare Pt/C catalyst was also studied. Prior the FCs measurement, the Gas Diffusion Electrodes (GDE), containing the composite catalysts, were characterized by infrared spectroscopy (Figure S4). For comparison purpose, the infrared spectrum of a home-made Nafion membrane (see Experimental) was also recorded. The two main peaks around 1230 and 1153 cm^{-1} can be assigned to the asymmetric and symmetric CF stretching vibrations of Nafion, ν_{as}(CF) and ν_s(CF). In this region, the asymmetric SO stretching vibration, ν_{as}(SO), usually occurring in the 1350–1250 cm^{-1} range, is also found, that overlaps with the CF stretching.[52] Together with these signals, the Pt/C:CeO$_2$ 1:0.5 and Pt/C:CeO$_2$ 1:1 samples show, as expected, additional bands due to CeO$_2$ (see Figure 3), confirming the presence of the additive. Furthermore, the main peaks around 1200 cm^{-1} are shifted to smaller wavenumbers, confirming a local interaction within the Nafion-based composite electrodes. In fact, this shift can be attributed either to the interaction of the electrocatalyst with Nafion or to the hydration grade of the polymer.[53]

PEM fuel cell performances were evaluated at 80 °C, moving from 31 % and 81 % relative humidity; moreover, practical desirable conditions of 31 % RH and high temperature (110 °C) were investigated. As reported in Figure 7a, in contrast with RDE experiments, better fuel cell performances under 31 % RH and T = 80 °C are obtained with the Pt/C:CeO$_2$ 1:0.5-based MEA
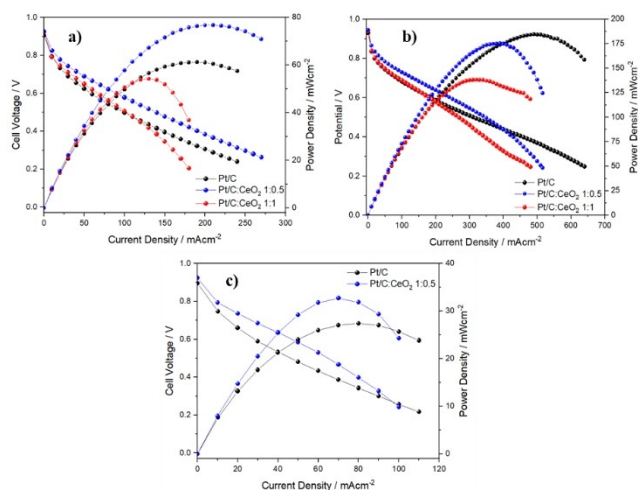

Figure 7. Comparison of fuel cell performances at a) 31 % RH and T = 80 °C; b) 81 % RH and T = 80 °C c) 31 % RH and T = 110 °C.

in terms of OCV (Open Circuit Voltage), maximum current and power delivered, confuting the previous hypothesis where the Pt/C:CeO$_2$ 1:1 sample was addressed as the best composition.

The Pt/C:CeO$_2$ 1:1-based MEA showed a good performance with respect to bare Pt/C, only in the activation region of the polarization curve, whereas at higher current density, a larger mass diffusion over-potential became predominant, as visible from the slope changes of the curve. The presence of a high content of hygroscopic cerium oxide at the cathode side seems to promote the flooded electrode phenomena. Water molecules produced during the oxygen reduction reaction could be strongly retained on the oxide surface causing a mass diffusion over-potential because of the waterlogged electrode, consequently the charge-transfer resistance to the cathode side results significantly increased. Meanwhile, when the amount of cerium oxide is low (Pt/C:CeO$_2$ 1:0.5-based MEA) the high hygroscopicity of CeO$_2$ allows to maintain a good hydration grade of the electrode surface, sustaining fuel cell performances. Indeed, at these operating conditions, this composite electrode based on Pt/C:CeO$_2$ 1:0.5 delivers higher current and power densities with respect to the other samples. These aspects are highlighted in the Nyquist plots of the impedance spectra (Figure S5), recorded during fuel cell operations at 0.6 V. The ohmic resistance of the cell and the electrode charge-transfer resistance were evaluated by using the following equivalent circuit R$_\Omega$(R$_{ct,1}$Q)(R$_{ct,2}$Q). In details, R$_\Omega$, which corresponds to the intercept on the real axis in the higher frequency region, is the ohmic resistance, Q is the phase constant element, and R$_{ct,1}$ and R$_{ct,2}$ are the charge transfer resistances which reflect the diameter of semi-circles in the mid and lower frequency regions, respectively. By comparing all the samples studied, the composite Pt/C:CeO$_2$ 1:0.5-based MEA shows lower resistance values, justifying the best fuel cell performance obtained. To highlight this interesting aspect, the membrane internal resistance was estimated by using the current interrupt method (Figure S6). Based on the R$_\Omega$ values obtained, the ionic conductivity (σ) was estimated for each sample and reported in

ChemElectroChem

Research Article
doi.org/10.1002/celc.202300168

**Chemistry
Europe**
European Chemical
Societies Publishing

the same Figure S6.[54] If one considers that the electrolyte used is always a commercial Nafion membrane, the lower ohmic resistance obtained when both composite catalysts are used, with respect to bare Pt-based fuel cell, is clearly due to the presence of the hygroscopic cerium oxide at the cathode side.

The capability of this inorganic additive to absorb and retain water by the presence of hydroxyl groups on the surface of the oxide was demonstrated by Wang and coworkers, who observed that the addition of Pt/CeO_2 particles directly into a Nafion membrane can catalyze the H_2 and O_2 crossover to generate water for self-hydrating the membrane, improving the fuel cell performances under low humidity.[55] Recently, we reported a study about a sub-stoichiometric perovskite, $CaTiO_{3-\delta}$, used as additive in Nafion membranes, demonstrating that the presence of defects on the perovskite surface can act as active sites for the absorption of water, increasing the proton conductivity of composite membranes especially at higher temperature and reducing the drawback of membrane dehydration at those temperatures.[56,57]

It is reasonable to assume that, in our case, the oxygen vacancies on cerium oxide surface, holding water molecules on the electrode, induce an extra hygroscopicity on Nafion membrane promoting more efficient ion transfer across the interface membrane-electrode and within the catalyst layer itself (where the ionomer is present), thus increasing the ionic conductivity of Nafion. This behavior of cerium oxide has not been reported to date.

In order to understand in depth, the role of water inside the fuel cell, measurements at high relative humidity (81%) were carried out. As shown in Figure 7b, $Pt/C:CeO_2$ 1:0.5-based MEA preserves its better performance, showing a lower loss potential in the activation region of polarization curve. Unfortunately, at intermediate-high current densities, a change in the polarization curve slope is observed, due to mass diffusion overpotentials. At these condition of high RH, $Pt/C:CeO_2$ 1:0.5-based MEA starts suffering from the high water content produced at the cathode side, which results in an excessive mass transport constrains. As expected, great charge transfer resistances are associated to $Pt/C:CeO_2$ 1:1 sample which, having the highest amount of additive, gives rise to flooded-electrode phenomena already at about 250 $mA\,cm^{-2}$. On the contrary, benchmark Pt/C-based MEA exhibits higher power and current densities because of a better water distribution in the catalyst layer.

From the Nyquist plots in Figure S5b, even though higher charge resistances are detected at low frequencies for both composite samples, a good ohmic resistance, ascribed to the intercept at high frequency, is maintained in the $Pt/C:CeO_2$ 1:0.5-based MEA. The current interrupt measurements shown in Figure S6b confirm the better results in terms of lower ohmic resistance and higher ionic conductivity for this composite MEA containing $Pt/C:CeO_2$ 1:0.5 up to 500 $mA\,cm^{-2}$, beyond which mass-diffusion overpotential start affecting the cell performances.

Under practical and more stringent conditions of 110°C and 31% RH, applied for the fuel cell tests reported in Figure 7c, the composite $Pt/C:CeO_2$ 1:0.5-based MEA maintains better performance with respect to the bare Pt/C-based MEA, exhibiting higher power density, most likely due to traces of surface water still present on the cerium oxide surface. At these critical conditions of low RH and high temperature, the $Pt/C:CeO_2$ 1:1-based MEA didn't give acceptable performance, probably due to excessive mass transport constrains.

As shown from the Nyquist plots in Figure S5c, a good charge-transfer resistance is maintained in the $Pt/C:CeO_2$ 1:0.5-based MEA with respect to Pt/C sample, highlighting again how the addition of this hygroscopic cerium oxide serves in boosting the ORR kinetics favoring the oxygen gas passage on the electrode surface. All resistance values evaluated by Nyquist plots, at the various fuel cell operating conditions explored in this work, are summarized in Table S1. These results underline a strong dependance on the concentration of cerium oxide, which, having high hygroscopicity, impacts differently on the electrochemical performances according to the fuel cell operating conditions. The best performance are obtained for composite $Pt/C:CeO_2$ 1:0.5 cathode under high temperature and low relative humidity, demonstrating the applicability of the proposed catalyst in PEM fuel cell under desired critical conditions. More detailed studies to understand the surface chemical behavior of cerium oxide additive, and the stability of composite $Pt–CeO_2$ catalysts, could be useful to tailor and emphasize the application in polymer electrolyte membrane fuel cells devices.

Conclusion

In this work a template-driven sol-gel process was developed to obtain highly hydrophilic cerium oxide nanoparticles. This compound was used as additive to platinum for the oxygen reduction reaction in acidic media. Two composite catalysts with different amount of oxide, i.e. $Pt/C:CeO_2$ 1:0.5 and $Pt/C:CeO_2$ 1:1, were prepared and compared to a commercial Pt/C catalyst used as reference. Both composite catalysts show an homogeneous distribution of the ceria additive, as well as superior electrochemically active surface area and oxygen reduction activity in comparison with benchmark Pt/C. RDE measurements revealed that the $Pt/C:CeO_2$ 1:1 catalyst possesses the best activity, allowing a 4e⁻ reduction pathway for the ORR. However, fuel cell tests, combined with impedance studies, at 31% RH and temperatures from 80°C to 110°C, recognize in the $Pt/C:CeO_2$ 1:0.5 composition the beneficial effect of cerium oxide, in terms of higher current/power densities, lower charge-transfer resistance and reduced ohmic resistance. This enhancement, revealed under critical fuel cell working conditions for the quoted composite catalyst, is interpreted as a compromise between the improved ORR activity, due to CeO_2 additive, and its high hygroscopicity, that must be balanced to guarantee the right hydration degree at the cathode ensuring a good membrane-electrode interface contact. Overall, the key role of the cerium oxide as an effective electrode component for the ORR in PEM fuel cell systems was demonstrated, highlighting the existence of a critical additive concentration. When the inorganic compound is added in a

proper amount with respect to platinum, low relative humidity and high temperature PEMFC operations are allowed.

Experimental Section

A hydrothermal synthesis was developed to obtain cerium oxide (CeO_2) starting from cerium(IV) hydroxide, and Pluronic F127 as precursor and structure-directing agent respectively. In particular, according to the following procedure, Pluronic F127 was mixed with absolute ethanol in vigorous stirring for 20 min at 35 °C. Subsequently, cerium hydroxide was added to the above solution obtaining its completely dissolution at 60 °C after 45 min. A 3 M NaOH solution was dropped into the mixture to adjust the pH value at 12; in this alkaline environmental the conversion to CeO_2 occurred. Afterwards, the solution was transferred in an autoclave, and it was treated at 180 °C for 24 h followed by natural cooling to room temperature. The solid product was centrifuged and washed several times with bi-distilled water in order to remove all impurities. Finally, the oxide was calcined for 3 h at 550 °C (heat rate 3 °C/min). All reagents used were Sigma Aldrich products.

A Nafion membrane was prepared from the Nafion 5 wt.% dispersion (E.W. 1100, Ion Power Inc, München Germany), according to the following procedure reported elsewhere.[54,56] The Nafion dispersion was heated at 80 °C to gradually replace the solvents, water and alcohols, with N,N-dimethylacetamide ($> 99.5\%$, Sigma Aldrich, St. Louis, MO, USA) at 80 °C. Afterwards, the solution obtained was casted on a Petri dish and dried at 80 °C overnight. Finally, the membrane was hot-pressed at 50 atm, 175 °C for 15 min and was finally activated in boiling 3% w/w hydrogen peroxide (H_2O_2, 34.5%–36.5%, Sigma Aldrich, St. Louis, MO, USA), H_2SO_4 (0.5 M) and distilled water.

X-ray diffraction (XRD) analysis was performed to study the phase of the prepared inorganic compound, using a Rigaku D-Max Ultima +diffractometer, equipped with a Cu Kα radiation source and graphite monochromator, in the 2θ range 20–90°. The average crystallite size of the oxide was calculated using the Maud code.

N_2-adsorption experiments were used for the determination of pores size distribution and for the evaluation of the specific surface area of the cerium oxide by the Brunauer-Emmett-Teller (BET) equation using a Micromeritics ASAP 2010.

Through high-resolution field emission scanning electron microscopy (HR-FESEM)+EDS (Energy Dispersive X-ray Spectroscopy) analysis, the morphological structure of the additive and catalyst inks were evaluated using an Auriga Zeiss instrument at the Interdepartmental Research Center on Nanotechnologies applied to Engineering (CNIS) of Sapienza University of Rome.

Vibrational spectroscopy studies were carried out by Attenuated Total Reflectance – Fourier Transform Infrared (ATR-FTIR). The spectra were collected with a PerkinElmer 2000 FTIR spectrometer recording 240 scans for each sample at ambient temperature in the range of 400–4000 cm^{-1}.

Vibrational spectroscopy studies on the gas diffusion electrodes and Nafion membrane were carried out using a Bruker LUMOS II FTIR micro-spectrometer in reflection mode, recording 2048 scans for each sample at ambient temperature in the range of 450–2000 cm^{-1}.

Raman spectroscopy was performed using a DILOR LabRam HR Raman Microscopy with a He–Ne (632.9 nm) laser source and a CCD Peltier-cooled detector.

To determine the thermal stability of the sample, thermal gravimetric analysis (TGA) was carried out with a TGA2 (Mettler-Toledo, Zaventem, Belgium) under air flux (80 mL/min) from 25 °C to 400 °C at a scan rate of 10 °C/min. TGA was also used to evaluate the Oxygen Capacity Storage (OCS) of the cerium oxide; the sample was tested in the temperature range from 25 °C to 200 °C with the following protocol: the oxide was preliminarily heated from 25 °C to 200 °C under nitrogen flux to remove all physiosorbed water and free oxygen in the sample; then, in the same atmosphere, the temperature was heated back to 25 °C and finally the powder was subjected at the same heating scan, from 25 °C to 200 °C, under air atmosphere.[58]

The oxygen reduction reaction of the catalysts were performed using a three-electrode cell set-up equipped with an Hg/Hg_2SO_4 (Amel 383/SHG/12J) reference electrode, a glassy carbon (GC, geometric surface area $A = 0,126$ cm^2) working electrode and a Platinum wire counter electrode. With the aim to optimize the uniformity of the current density distribution, the reference electrode was connected to the electrolyte via a Luggin capillary probe placed close to the working electrode. A 0.1 M $HClO_4$ solution was used as electrolyte. Three different catalytic compositions have been prepared and compared, i) Pt/C, with 20 wt.% Pt content with respect to C (BASF Fuel Cell, Inc), ii) Pt/C+CeO_2, with Pt:CeO_2 1:0.5 weight ratio, iii) Pt/C+CeO_2, with Pt:CeO_2 1:1 weight ratio. To obtain homogeneous catalytic inks, a suspension of Pt/C or Pt/C+CeO_2 powder and 5 wt.% Nafion solution (E.W. 1100, Ion Power Inc, München, Germany) was prepared in isopropyl alcohol and it was sonicated in an ultrasonic water bath for 30 min. The final ink was dropped onto a GC disk electrode leading to a Pt loading equal to 25 µg cm^{-2} for each sample. The GC was pre-cleaned by a dispersion aluminium oxide (20 wt.% in water, Sigma Aldrich). The electrochemical measurements were performed with a BiStat potentiostat (Bio-Logic Science Instruments). All catalytic compositions were subjected to an activation procedure consisting of 50 voltammetric cycles (CV) under nitrogen atmosphere at a scan rate of 50 mV s^{-1}; subsequently, five potential cycles were performed at a scan rate of 20 mV s^{-1} in the potential range from 0.05 to 1.2 V vs. reference hydrogen electrode (RHE) to evaluate the electrochemically active surface area (ECSA). The oxygen reduction reaction (ORR) activity was studied by means of linear sweep voltammetry (LSV) after saturating the electrolyte solution with O_2 for 30 min. The LSV curves were evaluated in the potential range from 1.2 to 0.2 V vs. RHE, at a scan rate of 5 mV s^{-1} using a rotating disk electrode (RDE) at different rotations speeds (400, 600, 900, 1200, 1600 and 2500 rpm).

According with the well-known Koutecky–Levich (K–L) equation, here reported (Eq. 1):

$$\frac{1}{j} = \frac{1}{j_k} + \frac{1}{j_d} = \frac{1}{j_k} + \frac{1}{0.62 nFC_{O_2} D_{O_2}^{2/3} v^{-1/6} \omega^{1/2}} \qquad (1)$$

the electron transfer number per O_2 molecule was estimated; all the parameters used to calculate this value are referred to the 0.1 M $HClO_4$ solution, as reported in literature.[59]

Three membrane-electrode assemblies (MEAs) were realized by depositing through a brushing technique the catalytic ink onto dry carbon cloth gas diffusion layers (GDL, ElectroChem. Inc.). The catalyst slurry was prepared with Platinum supported on carbon, (20 wt.% Pt/C, BASF Fuel Cell, Inc), Nafion solution (5% w/w E.W. 1100, Ion Power Inc, München, Germany), glycerol (Sigma Aldrich) and tetrabutylammonium hydroxide solution (1 M in methanol, TBAOH, Sigma Aldrich). To prepare the composite cathode catalysts, the cerium oxide powder was added into the above solution in a proper amount to reach the same compositions studied by RDE

ChemElectroChem

Research Article
doi.org/10.1002/celc.202300168

Chemistry Europe
European Chemical
Societies Publishing

experiments, i.e., Pt/C+CeO$_2$with Pt/C:CeO$_2$=1:1 weight ratio and Pt/C+CeO$_2$with Pt/C:CeO$_2$=1:0.5 weight ratio. The obtained suspension was deposited onto the GDL (5 cm^2 of active area) in order to achieve 2.5±0.3 mg cm^{-2} Pt loading on the resulting gas diffusion electrode (GDE). The membrane, employed for the Fuel Cell measurements, was a commercial Nafion 117 (Ion Power Inc, München, Germany). Before to realize the membrane-electrode assembly (MEA), both electrodes and Nafion membrane were activated sequentially with a 3 wt.% H$_2$O$_2$, 0.5 M H$_2$SO$_4$ and distilled water at 80°C for 2 h.[60] Finally, the assembly was made by hot pressing the membrane between the electrodes at 120°C and 2 tons for 7 min. The electrochemical evaluations of the MEAs were carried out with a single cell connected to a compact fuel cell system (850 C, Scribner Associates Inc, Southern Pines, NC, USA), feeding fully humidified hydrogen (150 mL min^{-1}) and air (700 mL min^{-1}) at anode and cathode respectively under atmospheric pressure. In situ electrochemical impedance spectroscopy (EIS) was performed with the 880 Impedance Analyzer in the 10 KHz–1 Hz frequency range considering an amplitude of the sine wave of 10% of the DC current present at 0.6 V cell voltage. The performance of each MEA was measured at 80°C and 110°C and relative humidity of 31%.

Acknowledgements

Conflict of Interests

The authors declare no conflict of interest.

Data Availability Statement

The data that support the findings of this study are available from the corresponding author upon reasonable request.

Keywords: CeO$_2$ · electrocatalysts · oxygen reduction reaction · PEM fuel cell.

[1] I. Staffell, D. Scamman, A. Velazquez Abad, P. Balcombe, P. E. Dodds, P. Ekins, N. Shah, K. R. Ward, *Energy Environ. Sci.* **2019**, *12*, 463–491.
[2] E. S. Hanley, J. P. Deane, B. P. O'Gallachòir, *Renewable Sustainable Energy Rev.* **2018**, *82*, 3027–3045.
[3] F. H. Sobrino, C. R. Monroy, J. L. H. Perez, *Renewable Sustainable Energy Rev.* **2010**, *14*, 772–80.
[4] T. Abbasi, S. A. Abbasi, *Renewable Sustainable Energy Rev.* **2011**,*15*, 3034–3040.
[5] R. E. Rosli, A. B. Sulong, W. R. W. Daud, M. A. Zulkifley, T. Husaini, M. I. Rosli, E. H. Majlan, M. A. Haque, *Int. J. Hydrogen Energy* **2017**, *42*, 9293–9314.
[6] R. K. Ahluwalia, X. Wang, R. Kumar, *J. Power Sources* **2008**, *177*, 167–176.
[7] S. Siracusano, C. Oldani, M. A. Navarra, S. Tonella, L. Mazzapioda, N. Briguglio, A. S. Aricò, *J. Membr. Sci.* **2019**, *578*, 136–148.
[8] M. Zaton, J. Roziere, D. Jones, *Sustain. Energy Fuels* **2017**, *1*, 409–438.
[9] Z. B. Wang, P. J. Zuo, Y. Y. Chu, Y. Y. Shao, G. P. Yin, *Int. J. Hydrogen Energy* **2009**, *34*, 4387–4394.
[10] D. Cozzi D, C. De Bonis, A. D'Epifanio, B. Mecheri, A. C. Tavares, S. Licoccia, *J. Power Sources* **2014**, *248*, 1127–1132.
[11] C. Lim, L. Ghassemzadeh, F. Van Hove, M. Lauritzen, J. Kolodziej, G. G. Wang, S. Holdcroft, E. Kjeang, *J. Power Sources* **2014**, *257*, 102–110.
[12] Z. Zheng, F. Yang, C. Lin, F. Zhu, S. Shen, G. Wei, J. Zhang, *J. Power Sources* **2020**, *451*, 227729–227738.
[13] C. Chen, G. Levitin, D. W. Hess, T. F. Fuller, *J. Power Sources* **2007**, *169*, 288–295.
[14] S. Xiao, H. Zhang, C. Bi, Y. Zhang, Y. Zhang, H. Dai, Z. Mai, X. Li, *J. Power Sources* **2010**,*195*, 5305–5311.
[15] A. Ohma, S. Yamamoto, K. Shinohara, *J. Power Sources* **2008**, *182*, 39–47.
[16] K. Ketpang, K. Lee, S. Shanmugam, *ACS Appl. Mater. Interfaces* **2014**, *6*, 16734–16744.
[17] M. Vinothkannan, S. Ramakrishnan, A. R. Kim, H.-K. Lee, D. Jin Yoo, *ACS Appl. Mater. Interfaces* **2020**, *12*, 5704–5716.
[18] W. Zhao, T. Haolin, Z. Huijie, L. Ming, C. Rui, X. Pan, P. Mu, *J. Membr. Sci.* **2012**, *421–422*, 201–210.
[19] W. Pengtao, C. Chao, T. Jinting, P. Mu, *Int. J. Hydrogen Energy* **2021**, *46* 34867–34873.
[20] A. M. Baker, S. M. Stewart, P. K. Ramaiyan, D. Banham, Y. Siyu, F. Garzon, R. Mukundan, R. L. Borup, *J. Electrochem. Soc.* **2021**, *168* 024507–024516.
[21] P. Dutta, S. Pal, M. S. Seehra, Y. Shi, E. M. Eyring, R. D. Ernst, *Chem. Mater.* **2006**, *18*, 5144–5146.
[22] H. Zhong, L. A. Estudillo-Wong, Y. Gao, Y. Feng, N. Alonso-Vante, *J. Energy Chem.* **2020**, *59*, 615–625.
[23] N. Pongpichayakul, S. Themsirimongkon, S. Maturost, K. Wangkawong, L. Fang, B. Inceesungvorn, P. Waenkaew, S. Saipanya, *Int. J. Hydrogen Energy* **2021**, *46*, 2905–2916.
[24] S. Sulekar, M. Mehr, J. H. Kim, J. C. Nino, *Inorganics* **2021**, *9*, 63–75.
[25] T. Mori, K. Tong, S. Yamamoto, T. Chauhan, T. Kobayashi, N. Isaka, G. Auchterlonie, R. Wepf, A. Suzuki, S. Ito, F. Ye, *ACS Omega* **2022**, *7*, 25822–25836.
[26] V. Prabhakaran, V. Ramani, *J. Electrochem. Soc.* **2014**, *161*, F1-F9.
[27] V. D. Cong Tinh, D. Kim, *J. Membr. Sci.* **2020**, *613*, 118517–118526.
[28] C. J. Neal, C. R. Fox, T. Selvan Sakthivel, U. Kumar, Y. Fu, C. Drake, G. D. Parks, S. Seal, *ACS Nano* **2021**, *15*, 14544–14556.
[29] D. Andreescu, E. Matijevic, D. V. Goia, *Colloids Surf. A: Physicochem. Eng. Aspects* **2006**, *291*, 93–100.
[30] J. Calvache-Muñoz, F. A. Prado, J. E. Rodríguez-Páe, *Colloids Surf. A* **2017**, *529*, 146–159.
[31] N. W. Kim, D. K. Lee, H. Yu, *RSC Adv.* **2019**, *9*, 13829–13837.
[32] Z. Wu, M. Li, J. Howe, H. M. Meyer, S. H. Overbury, *Langmuir* **2010**, *26*, 16595–16606.
[33] F. Meng, L. Wang, *Mater. Lett.* **2013**, *100*, 86–88.
[34] D. W. Wheeler, I. Khan, *Vib. Spectrosc.* **2014**, *70*, 200–206.
[35] Z. V. Popovic, Z. Dohcevic-Mitrovic, A. Cros, A. Cantarero, *J. Phys. Condens. Matter* **2007**, *9*, 496209–496218.
[36] A. Z. Feng, F. E. Gabaly, X. Ye, Z. X. Shen, W. C. Chueh, *Nat. Commun.* **2014**, *5*, 4374–4382.
[37] B. Chen, Y. Ma, L. Ding, L. Xu, Z. Wu, Q. Yuan, W. Huang, *J. Phys. Chem. C* **2013**,*117*, 5800–5810.
[38] A. Migani, G. N. Vayssilov, S. T. Bromley, F. Illasac, K. M. Neyman, *Chem. Commun.* **2010**, *46*, 5936–5938.
[39] M. Miyauchi, A. Nakajima, T. Watanabe, K. Hashimoto, *Chem. Mater.* **2002**, *14*, 2812–2816.
[40] M. Xue, N. Peng, J. Ou, F. Wang, X. Li, W. Li, *Mater. Chem. Phys.* **2015**, *160*, 406–412.
[41] A. Tasdemir, B. Iskandarani, A. Yürüm, S. A. Gürsel, B. Y. Kaplan, *Int. J. Hydrogen Energy* **2021**, *46*, 32250–32260.
[42] K. Fugane, T. Mori, D. Rong Ou, P. Yan, F. Ye, H. Yoshikawa, J. Drennan, *Langmuir* **2012**, *28*, 16692–16700.
[43] T. Masuda, H. Fukumitsu, K. Fugane, H. Togasaki, D. Matsumura, K. Tamura, Y. Nishihata, H. Yoshikawa, K. Kobayashi, T. Mori, K. Uosaki, *J. Phys. Chem. C* **2012**, *116*, 10098–10102.
[44] T. Mori, D. R. Ou, J. Zou, J. Drennan, *Prog. Nat. Sci. Materials International* **2012**, *22*, 561–57.
[45] C. Durante, *Curr. Opin. Electrochem.* **2022**, *36*, 101119–1101129.
[46] M. Mazzucato, G. Daniel, V. Perazzolo, R. Brandiele, G. A. Rizzi, A. A. Isse, A. Gennaro, C. Durante, *Electrochem. Sci. Adv.* **2022**, 1–18.
[47] J. Wang, C. X. Zhao, J.-N. Liu, D. Ren, B.-Q. Li, J. Q. Huang, Q. Zhang, *Nano Mater. Sci.* **2021**, *3*, 313–318.
[48] D. H. Lim, W. D. Lee, D. H. Choi, H. I. Lee, *Appl. Catal. B* **2010**, *1–2*, 85–96.

[49] K. Fugane, T. Mori, D. R. Ou, A. Suzuki, H. Yoshikawa, T. Masuda, K. Uosaki, Y. Yamashita, S. Ueda, K. Kobayashi, N. Okazaki, I. Matolinova, V. Matolin, *Electrochim. Acta* **2011**, *56*, 3874–3883.

[50] M. Renzi, P. Mignini, G. Giuli, R. Marassi, F. Nobili, *Int. J. Hydrogen Energy* **2016**, *41*, 11163–11173.

[51] L. Mazzapioda, C. Lo Vecchio, A. S. Aricò, M. A. Navarra, V. Baglio, *Catalysts* **2019**, *9*, 1017–1027.

[52] A. Gruger, A. Regis, T. Schmatko, P. Colomban, *Vib. Spectrosc.* **2001**, *26*, 215–225.

[53] K. Kunimatsu, B. Bae, K. Miyatake, H. Uchida, M. Watanabe, *J. Phys. Chem. B* **2011**, *115*, 4315–4321.

[54] L. Mazzapioda, M. Sgambetterra, A. Tsurumaki, M. A. Navarra, *J. Solid State Electrochem.* **2021**, *26*, 17–27.

[55] L. Wang, S. G. Advani, A. Prasad, *ECS Electrochem. Lett.* **2014**, *3*, F30-F32.

[56] L. Mazzapioda, C. Lo Vecchio, O. Danyliv, V. Baglio, A. Martinelli, M. A. Navarra, *Polymer* **2020**,*12*, 2019–2033.

[57] L. Mazzapioda, M. A. Navarra, F. Trequattrini, A. Paolone, K. Elamin, A. Martinelli, O. Palumbo, *Membranes* **2019**, *9*, 143–155.

[58] Y. Nagai, T. Nonaka, A. Suda, M. Sugiura, *R&D Rev. Toyota CRDL* **2002**, *37*, 1–20.

[59] L. Mazzapioda, C. Lo Vecchio, A. Paolone, A. S. Aricò, V. Baglio, M. A. Navarra, *ChemElectroChem* **2019**, *6*, 5941–5945.

[60] S. Siracusano, V. Baglio, I. Nicotera, L. Mazzapioda, A. S. Aricò, S. Panero, M. A. Navarra, *Int. J. Hydrogen Energy* **2017**, *42*, 27851–2785.

RESEARCH ARTICLE

Cerium oxide particles for PEM fuel cells: A non-stoichiometric CeO₂ is here proposed as co-catalyst in combination with Pt for the ORR in acid media. Compared with previous studies about Pt/C:CeO₂ composite catalysts, the high hygroscopicity of CeO₂ plays a crucial role in optimizing the water drainage and the cathode/Nafion interface, resulting in a remarkable improvement in Nafion proton conductivity and in PEMFC performance at high temperatures (80 °C and 110 °C) and low relative humidity (31 %).
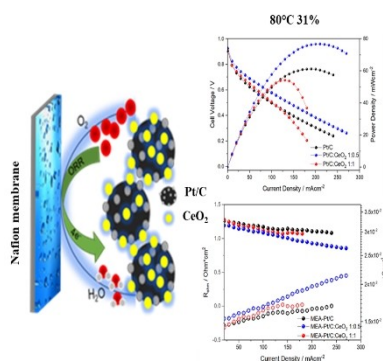
Dr. L. Mazzapioda*, G. Moscatelli, N. Carboni, Prof. S. Brutti, Prof. M. A. Navarra*

1 – 10

Super Hygroscopic Non-Stoichiometric Cerium Oxide Particles as Electrode Component for PEM Fuel Cells